Materials Today Bio 23 (2023) 100880

Contents lists available at ScienceDirect

Materials Today Bio

journal homepage: www.journals.elsevier.com/materials-today-bio

Shish-kebab structure fiber with nano and micro diameter regulate macrophage polarization for anti-inflammatory and bone differentiation

Gaowei Zhu [a], Rongyan Zhang [a], Qianyang Xie [b,**], Peilun Li [b], Fujun Wang [a], Lu Wang [a], Chaojing Li [a,*]

[a] Key Laboratory of Textile Science & Technology Ministry of Education, College of Textiles, Donghua University, Shanghai, 201620, China
[b] Ninth People's Hospital, College of Stomatology, Shanghai Jiao Tong University School of Medicine, and Shanghai Key Laboratory of Stomatology and Shanghai Research Institute of Stomatology, No. 639, Zhizaoju Rd., Shanghai, 200011, China

ARTICLE INFO

Keywords:
Macrophage polarization
Electrospinning fiber
Shish-kebab structure
Inflammatory response

ABSTRACT

Biopolymer grafts often have limited biocompatibility, triggering excessive inflammatory responses similar to foreign bodies. Macrophage phenotype shifts are pivotal in the inflammatory response and graft success. The effects of the morphology and physical attributes of the material itself on macrophage polarization should be the focus. In this study, we prepared electrospun fibers with diverse diameters and formed a shish-kebab (SK) structure on the material surface by solution-induced crystallization, forming electrospun fiber scaffolds with diverse pore sizes and roughness. *In vitro* cell culture experiments demonstrated that SK structure fibers could regulate macrophage differentiation toward M2 phenotype, and the results of *in vitro* simulation of *in vivo* tissue reconstruction by the microenvironment demonstrated that the paracrine role of M2 phenotype macrophages could promote bone marrow mesenchymal stem cells (BMSCs) to differentiate into osteoblasts. In rats implanted with a subcutaneous SK-structured fiber scaffold, the large-pore size and low-stiffness SK fiber scaffolds demonstrated superior immune performance, less macrophage aggregation, and easier differentiation to the anti-inflammatory M2 phenotype. Large pore sizes and low-stiffness SK fiber scaffolds guide the morphological design of biological scaffolds implanted *in vivo*, which is expected to be an effective strategy for reducing inflammation when applied to graft materials in clinical settings.

1. Introduction

Biomaterials are vastly used in medical diagnosis [1], health monitoring [2], drug delivery [3], and tissue repair and regeneration [4], and are especially vastly used for *in vivo* repair due to their porosity, flexibility, and facilitation of cell adhesion and proliferation [5]. However, when implanted, they can create *in vivo* wounds and elicit an immune response in the host. Specifically speaking, prolonged or unrestricted proliferation of pro-inflammatory cells can lead to excessive inflammatory responses or even the formation of fibrotic scarring surrounding biomaterial implants [6], blocking vital communication between the implant and the surrounding environment. This is detrimental to biomaterial-mediated tissue repair and regeneration and may ultimately lead to implant failure.

Macrophages play a dominant role in the inflammatory response and have been vastly used to study the immunomodulatory capacity of biomaterials [7]. Macrophages can be polarized into M1 phenotypes that secrete pro-inflammatory cytokines (iNOS, TNF-α, and IL-12) [8] and anti-inflammatory M2 phenotypes that secrete transforming growth factor (TGF-α) and IL-10 [9]. M2 macrophages play a significant role in the anti-inflammatory response and tissue reconstruction through immune regulation by modulating the Th2 anti-inflammatory response [10]. The timely conversion of M0 to M2 macrophages is the key to the success of implant transplantation. Macrophages have been demonstrated to polarize depending on the microenvironment in which they are located and can initiate inflammatory responses by recognizing diverse bacterial components through mechanisms such as pattern recognition receptors [11]. Macrophage adhesion infiltration is an inevitable process post-material implantation [12], and the inhibition of macrophage adhesion infiltration is no longer an effective strategy for avoiding chronic inflammation. Modulating the interaction between biomaterials and macrophages to induce M2 macrophage polarization

* Corresponding author.
** Corresponding author.
E-mail addresses: xieqianyang86@126.com (Q. Xie), lcj@dhu.edu.cn (C. Li).

https://doi.org/10.1016/j.mtbio.2023.100880
Received 12 September 2023; Received in revised form 15 November 2023; Accepted 22 November 2023
Available online 28 November 2023

has emerged as a prominent area of research [13]. Several crucial cytokines and signaling pathways are recognized for their ability to induce macrophage polarization. For instance, interferon-γ (IFN-γ) is associated with M1 polarization [14], whereas interleukin-4 (IL-4) and interleukin-13 (IL-13) are known to promote M2 polarization [15]. Furthermore, the surface microstructure of the material significantly influences macrophage polarization [16,17]. The structural aspects of the material, including fiber diameter, pore size, and their arrangement, represent potential targets for regulating macrophage polarization [18]. However, it remains uncertain whether adjustments in material stiffness, roughness, or pore size can effectively alter macrophage phenotype.

Electrospun fibers are vastly used as *in vivo* implant repair and replacement materials due to their high porosity and spatial interconnectivity [19–23], and electrospun fiber scaffolds best mimic the morphological and structural characteristics of the extracellular matrix (ECM) [24–26]. The regulation of macrophages by fiber morphology is a complex field involving the interactions of diverse factors, such as material type, material surface morphology, and physicochemical properties, including the microenvironment to which they are exposed [27–29]. Some studies have indicated that macrophages tend to adhere and cluster on rough hydrophilic surfaces (indentations, pits, and protrusions), polarizing either toward inflammatory M1 or anti-inflammatory M2 phenotypes, whereas others suggest that certain patterns and fiber topographies can induce macrophage polarization toward the M2 phenotype [30,31]. However, the mechanisms controlling macrophage polarization toward specific phenotypes remain obscure. Beyond morphology, the biomechanical characteristics of fiber scaffolds, such as bending stiffness and tensile properties, also influence macrophage behavior, including intercellular signaling and the release of bioactive molecules [32]. There is an urgent need to delve deeper into the relationship between fiber scaffolds and macrophages to better understand the mechanisms underlying macrophage polarization behavior. Polymeric materials are highly plastic, and their surface morphology can be modified by oxidation, coating, deposition, and plasma [33–35]. Solution-induced crystallization is a strategy for enhancing the mechanical attributes of fibers without altering their chemical attributes [36,37], which is a simple and easy process that does not require sophisticated instrumentation and has significant advantages in the formation of irregular surface morphologies for most *in vivo*-implanted degradable polymer materials [38,39].

Herein, we investigated the role of fiber characteristics (fiber diameter, roughness, stiffness, etc.) and the fiber topology aggregates in inducing macrophage polarization. Electrospinning fibers with 0.1–5 μm diameter and 1–15 μm pore diameter were prepared by electrospinning technology, and the solution-induced crystallization method was used to form a shish-kebab (SK) structure on the fiber surface, forming electrospinning fiber scaffolds with diverse pore diameter and roughness. We demonstrated the nanomorphology of the SK fiber scaffolds, which demonstrated a unique pattern in inducing adhesion protein unfolding, cell adhesion, and cytokine expression through *in vitro* macrophage coculture results. Next, we constructed a macrophage and stem cell coculture system to simulate the *in vivo* tissue reconstruction microenvironment, explored the effect of fiber scaffolds in the culture medium (CM) on the macrophage phenotype, and verified that M2 paracrine action promotes BMSCs differentiation into osteoblasts. Subcutaneous transplantation experiments in rats were conducted to verify whether the properties of the different structures of polycaprolactone (PCL) fiber scaffolds for inflammatory response and tissue regeneration *in vivo* were consistent with those *in vitro* (Scheme 1).

2. Materials and methods

2.1. Materials

PCL particles (MW:80,000 Da) were purchased from Sigma-Aldrich (St. Louis, MO, USA). N, N-dimethylformamide (DMF) and methanol (MeOH) were purchased from Sinopharm Chemical Reagent Co., Ltd. (Shanghai, China).

2.2. Preparation of electrospinning fiber scaffolds

To prepare polycaprolactone (PCL) fibers with diverse diameter distributions, two different solvent systems were prepared; the volume ratios of the spinning solvents are depicted in Table 1. A certain mass of PCL was dissolved in the above two solvent mixtures, and the mass

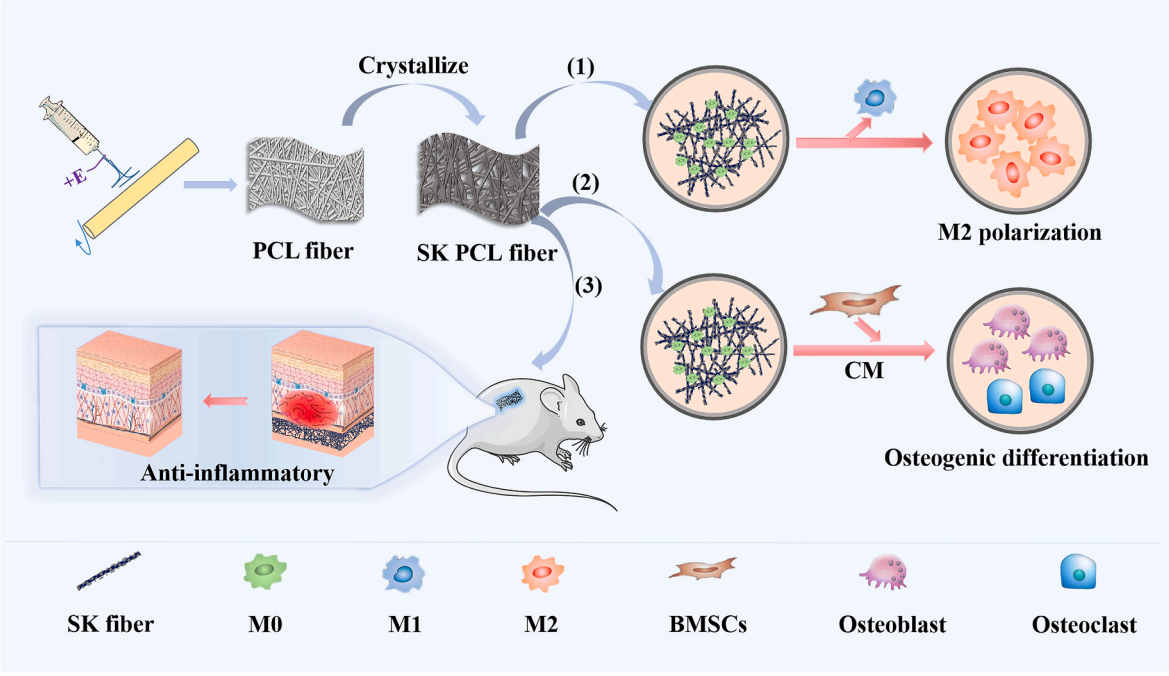

Scheme 1. Schematic diagram of the preparation and research idea of SK structured PCL fiber scaffold.

Table 1
Genes and the primers used in qPCR.

Genes	Forward primer sequence (5′–3′)	Reverse primer sequence (5′–3′)
Rat actin	TGACAGGATGCAGAAGGAGATTAC	GAGCCACCAATCCACACAGA
IL-10	GGGCTGCCTTCAGTCAAGTGAAG	GACAAGGCTTGGCAACCCAAG
IL-6	TACCACTTCACAAGTCGGAGGCT	TCTGACAGTGCATCATCGCTGTT

fractions of the PCL solutions are depicted in Table S1. The spinning solution is loaded in a 20 mL syringe, left to drain the air bubbles, and installed in the electrospinning machine; the relevant parameters of spinning: voltage of 20 kV, environmental parameters for the temperature of 22–25 °C, relative humidity of 30–40 %. After spinning, the fiber scaffolds were dried in a vacuum oven at 35 °C for 24 h to remove the residual solvent. Fiber scaffolds prepared from a weight percent of 10 wt % and 15 wt% PCL were denoted as P10 and P15.

2.3. Preparation of SK structured fiber scaffolds

Electrostatically spun fiber scaffolds were post-treated to obtain fibers with an SK structure. A water bath was heated to 60 °C for 2 h to dissolve PCL in amyl acetate, and a solution with a mass fraction of 0.5 % (m/v) PCL was prepared, cooled to room temperature (approximately 20 °C), and then 4 mL was incorporated dropwise to the 4 cm × 4 cm fiber scaffolds. After 40 min of treatment, the excess solution was rinsed off with amyl acetate, and the fiber scaffolds were placed in a fume hood to thoroughly air-dry. The fabricated fiber scaffolds were denoted as P10-SK and P15-SK.

2.4. Characterization of the physicochemical properties of fiber scaffolds

2.4.1. Surface micromorphology

The surface of the fiber scaffolds was gold-sprayed under vacuum, and the surface micromorphology of the fiber scaffolds was observed using a field-emission electron microscope (SU8010, Hitachi, Tokyo, Japan). The fiber diameters of the scaffolds were measured using ImageJ software (National Institute of Health, Bethesda, MD, USA). For each specimen, 100 fibers were selected for measurement and averaged. The surface roughness of single fibers of the fiber scaffolds was measured using atomic force microscopy (AFM) in a scanning range of 4 × 4 μm^2. The surface roughness parameters of the single fibers of the fiber scaffolds included the arithmetic mean height (Sa) and root mean square height (Sq).

2.4.2. Contact angle test

Static water contact angle testing of the fiber scaffolds was conducted using a contact angle tester (OCA15EC, Dataphysics, Stuttgart, Germany). A microsyringe was used to incorporate 2 μL ultrapure water dropwise to the surface of the fiber scaffolds, photograph the droplets formed on the surface, and process the captured imaging droplets using the operating software. Five points per specimen were randomly selected for measurements and averaged.

2.4.3. Aperture test

The pore size distributions of the specimens were determined using a porous material pore size analyzer (CFP- 1100AI, PMI, Ithaca, NY, USA).

2.4.4. Mechanical performance testing

Four types of fiber scaffold specimens were cut into 20 mm × 3 mm rectangles, and the fiber scaffolds were stretched using an electronic fabric strength machine (YG(B)026G-500, Da Rong Textile Co, Jiang Sheng, China). Each specimen was measured five times, and the average value was recorded.

2.5. In vitro immunological performance evaluation of fiber scaffolds

2.5.1. Protein adsorption test

Ten labeled small 1.5 mL centrifuge tubes were first prepared to prepare a standard solution of bovine serum albumin (BSA). The average absorbance value of each tube was calculated and the standard curve was plotted. The BSA standard solution was added to the well plates and incubated on a shaker for 12 h, so that the proteins were fully bound to the fiber scaffolds. After reaching the set time, the well plates were washed with PBS to remove the weakly adhered proteins. Then 1 % sodium dodecylbenzene sulfonate (SDBS) was added to the well plates to soak the fiber scaffolds to strip the adsorbed proteins. Then the BCA working solution and protein solution were mixed proportionally (10:1) and reacted in a shaker for a period of time, and then the absorbance value of each well was measured using an enzyme marker (562 nm). Finally, the amount of protein adsorbed per sample per unit area was calculated from the standard curve and sample area.

2.5.2. In vitro macrophage culture

For the cell culture experiment, RAW 264.7 macrophage cells were provided by the Cell Bank, Chinese Academy of Sciences (Shanghai, China). RAW 264.7 macrophage *in vitro* culture assay was used to assess the effect of the four fiber scaffolds on the immune cell behavior. The cell culture medium comprised 87 % DMEM (Gibco, Billings, MT, USA), 10 % FBS (Gibco), 1 % sodium pyruvate, 1 % glutamine (Gibco), and 1 % penicillin/streptomycin (Gibco). The cells were changed every day and passaged once every 3 days. Samples for the cell experiments were cut and placed in 24-well plates, pressed with sterilized steel rings, and placed in alcohol vats for overnight fumigation. Alcohol was removed by evaporation in a sterile environment for 24 h prior to cell growth, and the material was washed thrice with PBS. A cell suspension with a 1 × 10^4 cells/mL density was incorporated dropwise to each well of a 24-well plate containing the fiber scaffold samples and incubated for 1d and 3d, respectively, cytotoxicity was detected using cck8 and absorbance values of the samples were determined using enzyme labeling.

2.5.3. Macrophage immunofluorescence staining

After a predetermined time, 4 % paraformaldehyde (Biosharp, Hefei, China) was incorporated to fix the cells in the dark, followed by 0.3 % TritonX-100 (Yeasen, Shanghai, China) at room temperature, and 5 % BSA (Sigma-Aldrich, Beijing, China) was incorporated to close the plate. Alexa Fluor 647-labeled goat anti-rabbit IgG H&L primary antibody (Abcam, Cambridge, UK) (MMR antibody; 1:1000 dilution) was incorporated to bind overnight at 4 °C, and a drop of diluted fluorescent secondary antibody was incorporated to stain at room temperature and protected from light. Diluted FITC Phalloidin (Yeasen) solution was incorporated to stain the cytoskeleton, and DAPI (Solarbio, Beijing, China) was incorporated to re-stain the nucleus. The stained cells were observed using Confocal laser scanning microscopy. The mean optical density (MOD) of the macrophage marker MMR was determined using ImageJ software.

2.5.4. Live/dead staining of cells

Live/dead cell staining was conducted as follows: A cell suspension with a 1 × 10^5 cells/mL density was incorporated dropwise to each well of a 24-well plate containing the fiber scaffold samples and incubated for 1 day. After a predetermined time, the plate was washed for 5 min thrice with PBS. Staining was conducted according to the relevant steps of the Live/Dead Cell Staining Kit (KeyGen, Thermo Fisher Scientific, Waltham, MA, USA). Cells were stained using an inverted fluorescence microscope (Ti-s, Nikon, Tokyo, Japan).

2.5.5. Enzyme-linked immunosorbent assay (ELISA)

The concentrations of inflammation-associated cytokines were determined using an enzyme-linked immunosorbent assay (ELISA; Jingmei, China). A cell suspension with a 1 × 10^5 cells/mL density was

incorporated dropwise to each well of a 24-well plate containing the fiber scaffold samples and incubated for 1 day. The concentrations of TNF-α and IL-4 and anti-inflammatory factors IL-10 and IL-6 in the supernatant collected in the well plate were determined using ELISA kits. The wells were processed according to the relevant steps of the ELISA kit, the absorbance value of each well was measured using an enzyme marker, and the amounts of cytokines in the four fiber scaffolds were computed according to the standard curve.

2.6. Study of the behavior of combined immunomodulation on cells

In vitro co-culture experiments with stem cells were conducted to assess the characteristics of each fiber scaffold and the effect of macrophages on the osteogenic differentiation of stem cells. The cell culture medium used was the complete medium of rBMSCs (Gibco) from the Shanghai Cell Bank of the Chinese Academy of Sciences (Shanghai, China). The medium was changed once every 2–3 days according to the stem cell growth. The cells were cultured for 3–7 days and then passaged when the cells proliferated to 80–90 %. In this experiment, the 4th generation (P4) stem cells were selected to evaluate their osteogenic performance.

Fig. 4A depicts a schematic of the operational steps of the co-culture system (macrophages and stem cells). Macrophages were inoculated onto the fiber scaffolds of 6-well plates at a 3×10^5 cells/well density, and after incubation with the fiber scaffolds for 48 h, the supernatant was collected and subsequently filtered through a 0.22 μm filter membrane. Conditioned medium (CM) was prepared by mixing the filtered supernatant with complete stem cell medium at a ratio of 1:1. P4 stem cells were inoculated at a 2×10^3 cells density onto a 24-well plate without fiber scaffolds and cultured until the cells covered 80–90 % of the plate area. The CM was replaced with the osteogenic induction medium, and the culture was continued for 7 and 14 days with fluid changes every other day to observe the osteogenic differentiation of the stem cells in a timely manner.

ALP staining was used to evaluate the osteogenic activity of co-cultured stem cells. After reaching a predetermined time point, cells were washed thrice with PBS. Next, 4 % paraformaldehyde was incorporated into the cells. The fixative was aspirated for 3 h, washed thrice with PBS, and stained with ALP (Nanjing Jiancheng Bioengineering Institute, Nanjing, China) according to the manufacturer's instructions. After staining, the dye was aspirated, and the cells were washed thrice with deionized water. The specimens were observed under a light microscope. ALP quantification: After incubation for a set time, the plates were washed with PBS to remove free cells. The cell membranes were then permeabilized with TritonX-100. The liquid in the well plate was then transferred to a centrifuge tube and centrifuged at 13000×*g* for 15 min below 4 °C. The upper layer of the liquid was collected according to the ALP test kit, and the solution to be measured and the reagents were incorporated into the 96-well plate for quantification; the absorbance value of each well was measured with an enzyme marker (520 nm).

2.7. Investigation of inflammatory response subcutaneously in rats

All animal procedures were approved by the Ethics Committee of Donghua University for Experimental Animals (approval number: SYXK 2020-0018). SD rats were anesthetized by intramuscular injection of Sutex®50 (1 mL/kg body weight), and their backs were shaved and disinfected with 75 % alcohol. Six incisions of appropriate length were made on their backs with a surgical blade (the interval between incisions was greater than 1 cm), the specimens were implanted into the embedding bags using curved cuttings, and the wounds were closed with 3-0 sutures with stitches.

After reaching a predetermined time, SD rats were euthanized, the material and surrounding tissues were removed, rinsed with sterile saline, and 500 mg tissue was snap frozen in liquid nitrogen and stored at −80 °C in the refrigerator for qPCR assay. The remaining tissues and materials were stored in 4 % tissue fixative until subsequent tissue sectioning.

The removed tissues were fixed in 10 % neutral buffered formalin and subsequently embedded in paraffin, then made into 5 μm sections and stained sequentially with hematoxylin and eosin (HE; Solarbio) and Masson's trichrome (MT; Solarbio). Immunohistochemical staining included CD68 (Abcam; pan-macrophage marker) and CD206 antibody (Abcam; M2 phenotype macrophage marker). The tissue sections were stained using a biomicroscope. Image J was used to compute the number of macrophages and the image color pixel density (blue areas represent the deposited collagen of the tissues stained by MT). All images were acquired at a fixed distance of 100 μm from the tissue-fiber scaffold interface (n = 5).

The subcutaneous tissues around the fiber scaffolds were removed after 4 days for homogenization, mixed in the same group, and subjected to a quantitative polymerase chain reaction (qPCR) assay to isolate RNA, determine the amount and purity of RNA, and then reverse transcribed to synthesize cDNA. Target genes were IL-10 and IL-6, and the housekeeping gene Rat actin was used as an internal reference, and the expression levels of the target genes relative to the internal reference were computed according to the 2-ΔΔCt relative quantitative analysis.

2.8. Statistical analysis of data

The experimental data were expressed as "mean ± standard deviation," and one-way ANOVA and Turkey multiple comparison test were conducted using origin software. $p < 0.001$ (***), $p < 0.01$ (**), $p < 0.05$ (*) was considered a significant difference between the data.

3. Results and discussion

3.1. Preparation and characterization of electrospinning fibers and SK structures

Polycaprolactone (PCL) is a biodegradable polymer with excellent flexibility, processing properties, biocompatibility, and a vast range of applications in the medical field [40]. In this study, the PCL fiber scaffolds were prepared by electrospinning, as depicted in Table S1. Scaffolds with diverse fiber diameters and pore sizes were designed by varying the electrospinning parameters (solution mass fraction, pushing speed, receiving distance, and needle size) (Fig. 1A) with a flat and smooth fiber surface. The SK structure was constructed on the fiber surface using the solution-induced crystallization method, and SK-structured PCL fiber scaffolds with diverse diameters and pore diameters were obtained (Fig. 1A, bottom). Quantifying the fiber diameter (Fig. 1B), the average fiber diameter of P10 and P10-SK was small at 0.45 μm, the average fiber diameter of P15 and P15-SK increased to 2.84 μm with the increase of solution mass fraction and the adjustment of spinning parameters. The average pore diameter of P15 (12.50 μm) and P15-SK (11.57 μm) was significantly larger than that of P10 (3.10 μm) and P10-SK (1.78 μm) due to the decrease in fiber diameter and the increase in the interweaving points between fibers and the reduction in space (Fig. 1C). SEM images demonstrated that solution-induced crystallization on the fiber scaffolds formed a nanoscale SK structure with irregular folds and grooves, and the surface roughness of single fibers on the surface of the SK fiber scaffolds was tested using AFM (Fig. 1D). The distribution of the light-colored areas in Fig. 1D (a) depicts that the surface of both fiber scaffolds demonstrated high SK structure undulations with increased roughness. Fig. 1D (b) depicts the depth profiles of SK structures on the two fiber scaffolds and their Sa and Sq values. The heights of the undulations on the surfaces of the two SK-structured fiber scaffolds were 182, 216, and 177 nm, respectively, and the height and thickness of this sheet crystal were at the nanometer level, all of which can influence the cell adhesion behavior by interacting with cellular integrin clusters [41].

Solution-induced crystallization treatment changed the morphology

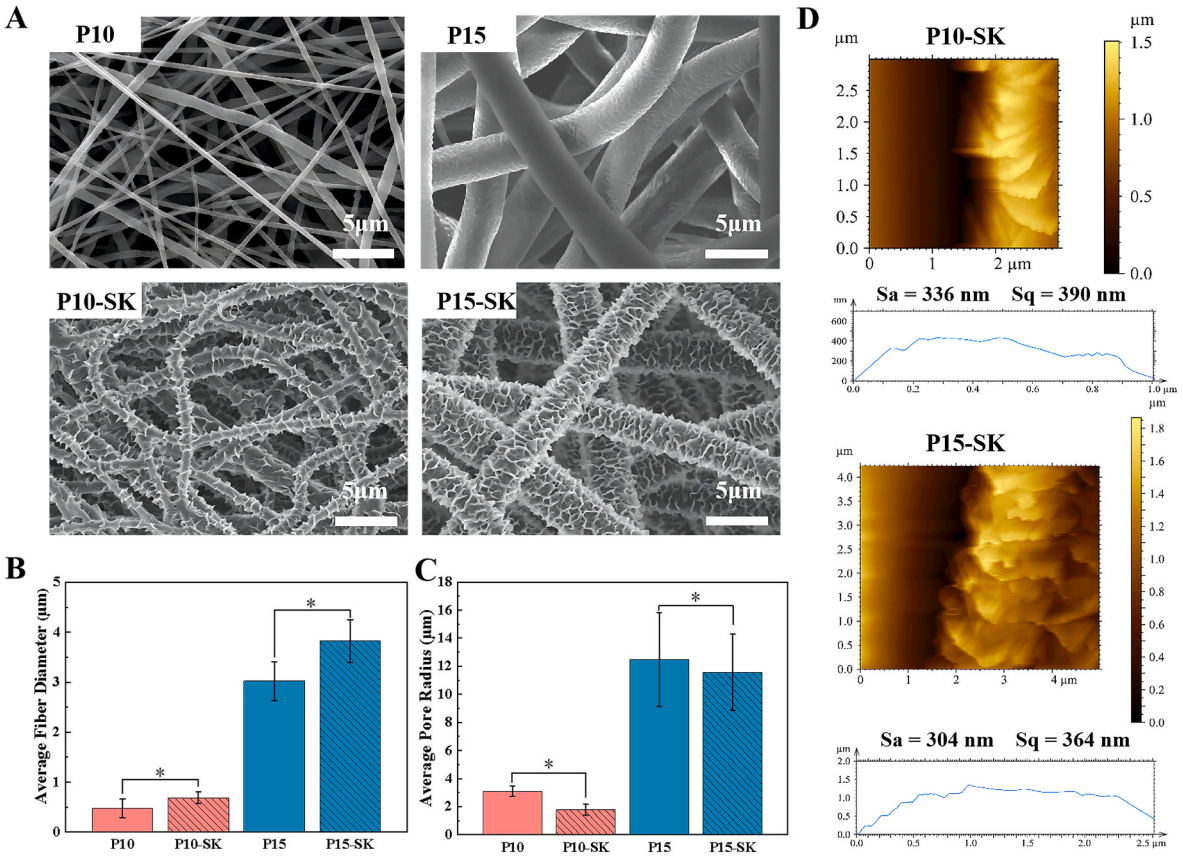

Fig. 1. Preparation and morphological characterization of PCL fiber scaffolds and their SK structures. (A) SEM of PCL (SK) fiber scaffolds, scale bar: 5 μm. (B) Fiber diameter distribution of fiber scaffolds, (C) Average pore size distribution of fiber scaffolds, (D) AFM morphology and depth profile of single fiber on the surface of fiber scaffolds with SK structure. *$p < 0.05$.

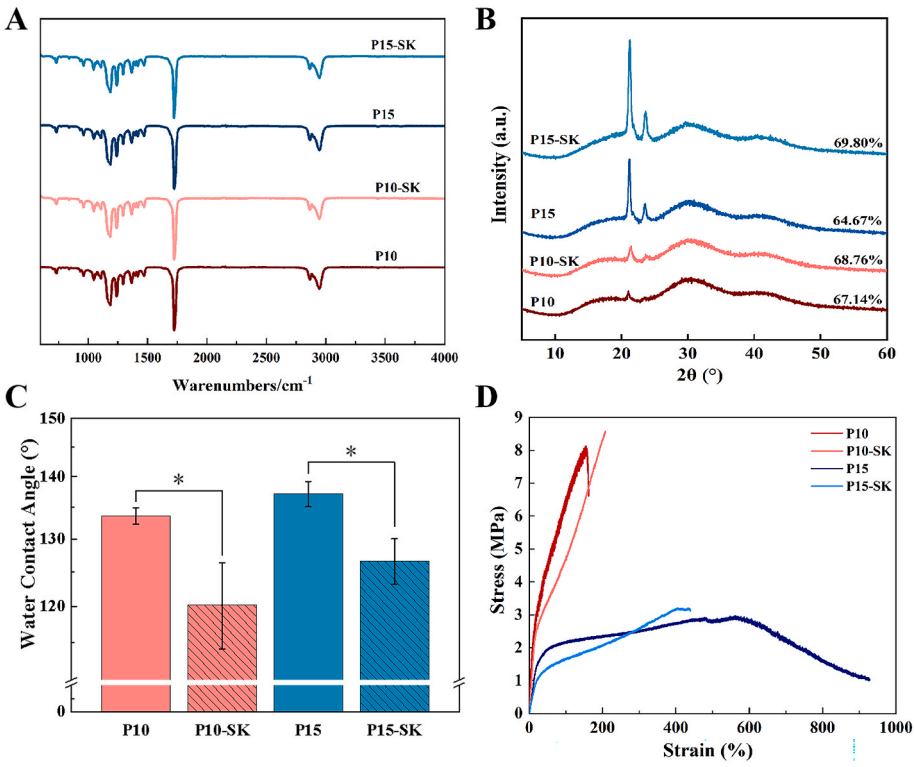

Fig. 2. Structural and performance characterization of PCL fiber scaffolds and their kebab structures. (A) FT-IR spectra and (B) X-ray diffraction of PCL fiber scaffolds and their tandem crystal structures. (C) Water contact angle test results of fiber scaffolds. (D) Tensile curve of fiber scaffolds. *$p < 0.05$.

of the fiber but did not change their composition, as can be seen from the infrared mapping of the fiber aggregates in Fig. 2 A. All fiber aggregates had the same composition, and no new bond formation was found. However, SK fiber's crystallinity increased by approximately 12°(Fig. 2 B) because solution-induced stringing is a phenomenon wherein crystalline polymers are induced to crystallize at temperatures lower than the usual Tg by the action of a supersaturated solution, wherein the crystalline polymers themselves are the solutes. Therefore, the SK fiber's composition did not change compared to that of the original fibers, whereas their crystallinity changed. The SK fiber structure influences its physical properties [42]. The water contact angle test of the fiber scaffolds (Fig. 2 C) indicated that all four fiber scaffolds exhibited hydrophobicity. Compared with flat-film scaffolds, such as P10 and P15, the nano-SK structure can improve the hydrophobicity of the fiber scaffold. The water contact angle of the P10-SK and P15-SK scaffolds with SK structures was significantly reduced. There is significant variability in the mechanical moduli of diverse ECM compositions, cells, and human tissues [43,44], and the mechanical properties of biomaterials are important parameters that affect cell fate and function [45]. Mechanical properties of PCL fiber scaffolds were tested (Fig. 2 D), and the tensile curves of the P15 group (P15, P15-SK) demonstrated low tensile strength (2.71 MPa) and high elongation (532.52 %) relative to the P10 group (P10, P10-SK), which is due to the thicker fibers of the P15 group (2.84 μm), fewer interweave points between fibers and fibers. This is because the P15 group fibers are thicker (2.84 μm) and have fewer interweave points between fibers; hence, the fibers can easily orient and slip along the interweave points and have high elongation. Additionally, the fiber scaffolds with the SK structure demonstrated a trend of greater breaking strength than the smooth fiber scaffolds, and the elongation at break demonstrated the opposite trend. This was probably because the SK structure on the fibers increased their roughness during the stretching process, which hindered the relative slip of the fibers and resulted in better mechanical properties. The elastic modulus of PCL fiber scaffolds with diverse structures depicted in Fig. S1 and the elastic modulus of fiber scaffolds with SK structure are all larger than those with smooth structure, which is in line with the analysis of changes in crystallinity.

3.2. Cell biocompatibility of the scaffolds

After implantation of the material in the body, the immune system rapidly responds by producing acute inflammation, recruiting large numbers of immune cells (granulocytes, mast cells, and monocytes) to the graft area and releasing large amounts of cytokines (IL-4 and TNF-α) to recruit more immune cells to the graft area. After 2–3 d, a chronic inflammatory response phase was observed [46]. In this study, the mouse macrophage cell line RAW264.7 was selected for co-culture with a fiber scaffold to verify the effect of fiber aggregate performance on macrophages. After 1 day of culture, the surface of the fiber scaffold demonstrated numerous live cells, and RAW264.7 grew in patches and was excited with distinct green fluorescence (Fig. S2). Conversely, there was little red fluorescence of dead cells, and the dead cells present can be considered as normal apoptosis, indicating the absence of cytotoxicity of the fiber scaffold. The depth of macrophage infiltration was further characterized, and macrophages reached the maximum infiltration depth (84.02 μm) on P15 (Fig. S3). With the largest pore size (12.50 μm) and the lowest stiffness (5.62 MPa), the large pore size facilitates macrophage infiltration and reduces the effect of the material on cell mechanics.

The pathogenesis of biomaterial-mediated immune responses is determined by the type of protein spontaneously adsorbed onto the surface of the biomaterial prior to immune cell recruitment. Moreover, the number of adsorbed proteins and their conformational changes depend on the surface properties of the biomaterial [47]. Therefore, we characterized protein adsorption on fiber scaffolds, and the results demonstrated that the SK structure facilitated protein adsorption on fiber scaffolds, and the protein adsorption of fiber scaffolds with SK structures (P10-SK, P15-SK) was greater than that of smooth fiber scaffolds (P10, P15), with the maximum adsorption of 123.90 μg/cm^2 for P15-SK (Fig. 3A). The synergistic effect of the SK structure of the fiber scaffold, large pore size, and low stiffness of the fiber aggregate on anti-inflammatory cytokines secretion was also investigated. Before proceeding, we conducted an assessment of the impact of fiber scaffolds on macrophage cell viability. Macrophages were co-cultured with the fiber scaffolds for one and three days. The results demonstrated that macrophages exhibited stable proliferation, with calculations indicating that the cell viability exceeded 85 % across all fiber scaffolds (Fig. 3B). Among all structural fibers, the pro-inflammatory factor IL-6 was secreted the least on the macroporous fiber scaffold P15-SK with an SK structure (42.76 μg/mL) (Fig. 3C). Similarly, less of the pro-inflammatory factor, TNF, was secreted on the surface of the P15-SK fiber scaffold than on the P10-SK scaffold (Fig. 3D). Interestingly, the large pore size and low stiffness of the fiber aggregates facilitated anti-inflammatory cytokines secretion. The anti-inflammatory factors IL-4 and IL-10 were secreted most frequently on the macroporous fiber scaffold P15-SK with SK structure, 122.89 μg/mL (Figs. 3E) and 43.85 μg/mL (Fig. 3F), respectively. SK fiber scaffolds showed a unique pattern of inducing adhesion protein unfolding, cell adhesion, and cytokine expression compared with smooth surfaces.

3.3. The SK structured fiber scaffolds induced polarization of RAW264.7 cells to M2 phenotype

We hypothesized that SKS-structured PCL fiber scaffolds would induce macrophage differentiation into the M2 phenotype and reduce the inflammatory response. We explored the inflammatory response of macrophages to the material by co-culturing macrophages with fiber scaffolds. Immunofluorescence staining of macrophages on the fiber scaffolds surface is depicted in Fig. 3. Macrophages produced the highest red fluorescence intensity on P15 at 4 h (Fig. 4A), indicating that M2 macrophages were the most polarized and that there was no difference in the fluorescence intensity of the other three fiber scaffolds. The fluorescence intensity of all samples diminished at 4 days (Fig. 4B), and the fluorescence intensity of M2-phenotype macrophages on the fiber scaffold was minimized in all cases. The expression of macrophage inflammatory factors was significantly reduced, and the MOD value data of the four samples at different time points verified this result (Fig. S4). The insignificant difference in fluorescence intensity between the fiber scaffolds at 4 days may be due to the difference between *in vitro* and *in vivo* situations, where macrophages must conduct complex physicochemical reactions *in vivo* with proteins of the complement system and lymphocytes of the adaptive immune system [48]. Additionally, considering the complex *in vivo* physiological environment and the singularity of the *in vitro* system that mimics acute inflammatory responses, the shortened duration and diminished effect of the fiber scaffolds resulted in inflammation that only demonstrated a different *in vivo* phase of the response. At this stage, the polarization of inflammatory cells resembles the later stages of a chronic inflammatory response [49]. Combined with the elastic modulus and pore size of the fiber scaffold described in the previous section, the combination of large pore size and low stiffness of the fiber aggregate favors macrophage polarization toward the M2 phenotype.

3.4. Effect of macrophage polarization on bone marrow stem cell differentiation

Mesenchymal stem cells (MSCs) play several roles in modulating the immune response to implanted materials, including direct involvement in the reconstruction of new tissues, paracrine secretion of cytokines, and stimulation of biochemical signaling pathways of the innate immune system to interact with immune cells [50–52]. Although we demonstrated the effect of SK-structured fiber scaffolds in inducing macrophage polarization toward the M2 phenotype, the complexity of

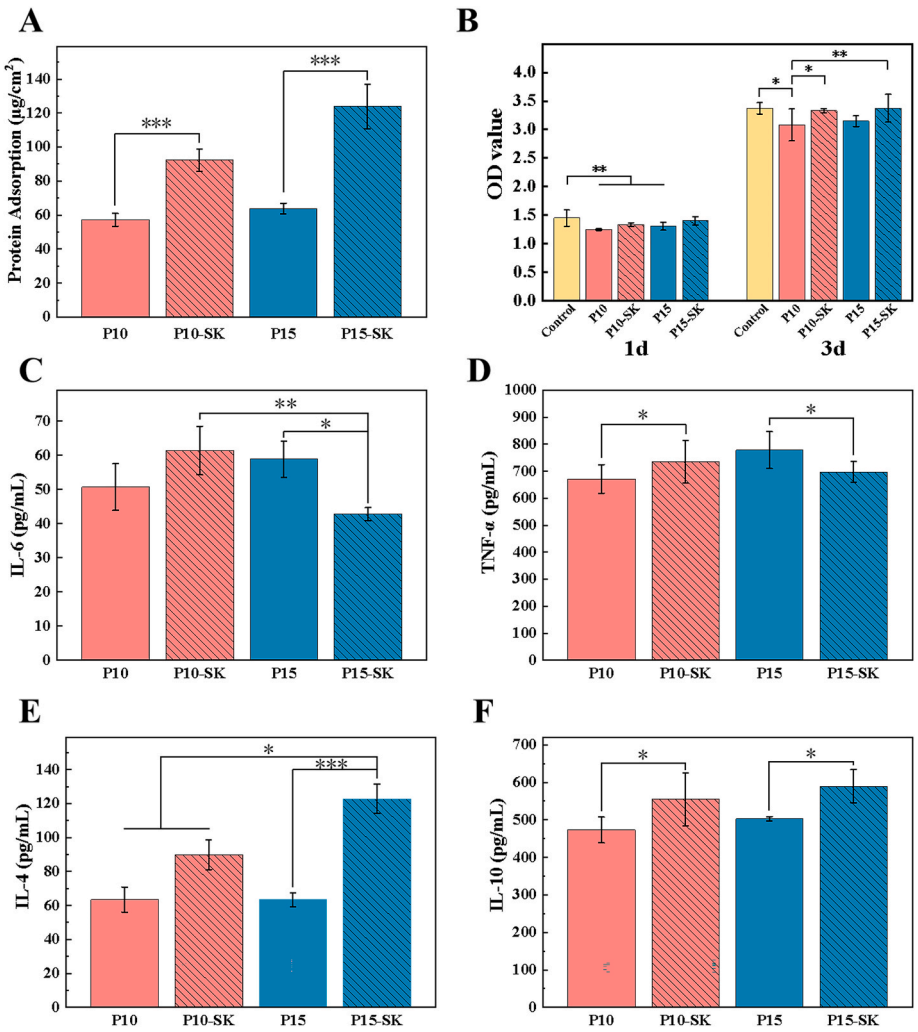

Fig. 3. Biocompatibility of diverse structured PCL fiber scaffolds. (A) Protein adsorption of diverse structured PCL fiber scaffolds. (B) Macrophage proliferation was assessed via CCK-8 assay after 1 and 3 days of cultivation on the fiber scaffolds (measured at 450 nm). (C–F) Secretion of pro-inflammatory cytokines IL-6(B) and TNF-α(C) on fiber scaffolds, and secretion of anti-inflammatory cytokines IL-4(D) and IL-10(E) on fiber scaffolds. *$p < 0.05$, **$p < 0.01$, ***$p < 0.001$.

the immune system microenvironment components and interactions is not sufficient to thoroughly demonstrate its effect. Therefore, to investigate the role of fiber-based materials in the co-culture system, a co-culture system of CM and rBMSCs with PCL fiber scaffolds cultured on macrophages was constructed (Fig. 4A), thus establishing the ecology between the fiber-based materials, immune response, and regenerating cells and exploring the effect of different fiber scaffold structures on macrophage differentiation and tissue reconstruction capacity by evaluating the osteogenic differentiation of stem cells after co-culture.

Staining for mineralized nodule formation in the co-culture system at 7 and 14 days (Fig. 5A), CM with diverse fiber scaffolds structures cultured with macrophages demonstrated the ability to continuously stimulate osteogenic mineralization of rBMSCs, and differential calcium nodule formation at 7 and 14 days indicated that CM could continuously stimulate stem cells differentiation to osteoblasts. As depicted in the ALP staining plot, The P15 group of fiber scaffolds exhibited higher ALP activity than the P10 group (Fig. 5B), which was more favorable for the osteogenic differentiation of rBMSCs. To demonstrate the pivotal role played by M2 macrophages, we utilized a CM devoid of macrophages to incubate fiber scaffolds with bone marrow mesenchymal stem cells for osteogenic differentiation. The results revealed that, at 7 and 14 days, only a minimal number of bone marrow mesenchymal stem cells underwent osteogenic differentiation, significantly lower than the experimental group containing macrophages (Fig. S5). Furthermore, to establish the impact of the fiber scaffold's structure on macrophage polarization, we performed morphological observations on the scaffolds after 7 and 14 days of co-culture. Scanning electron microscopy from Fig. S6 demonstrated that the fiber scaffold's structure remained unchanged during the culture process, and the SK structure underwent no alterations during incubation, providing evidence that the scaffold structure induced polarization of macrophages toward the M2 phenotype. Finally, combined with the quantitative ALP data analysis (Fig. 5C), CM with fiber scaffolds cultured with macrophages with SK structures exhibited higher ALP activity than the smooth structure, which was more conducive to the osteogenic differentiation of rBMSCs, ARS staining also confirmed the same research findings (see Fig. S7). The results of this system demonstrated that SK fiber scaffolds not only favored macrophage differentiation toward the M2 phenotype but also promoted stem cell differentiation toward osteoblasts by M2 macrophage paracrine effects.

3.5. *Fiber aggregate surface topology mediates resolution of inflammation in vivo*

To further investigate the *in vivo* immune response of the fiber scaffolds, a subcutaneous graft was conducted in SD rats, as depicted (Scheme 1), and evaluated for the acute (4 days) and chronic (14 days) phases of the inflammatory response, including tissue regeneration

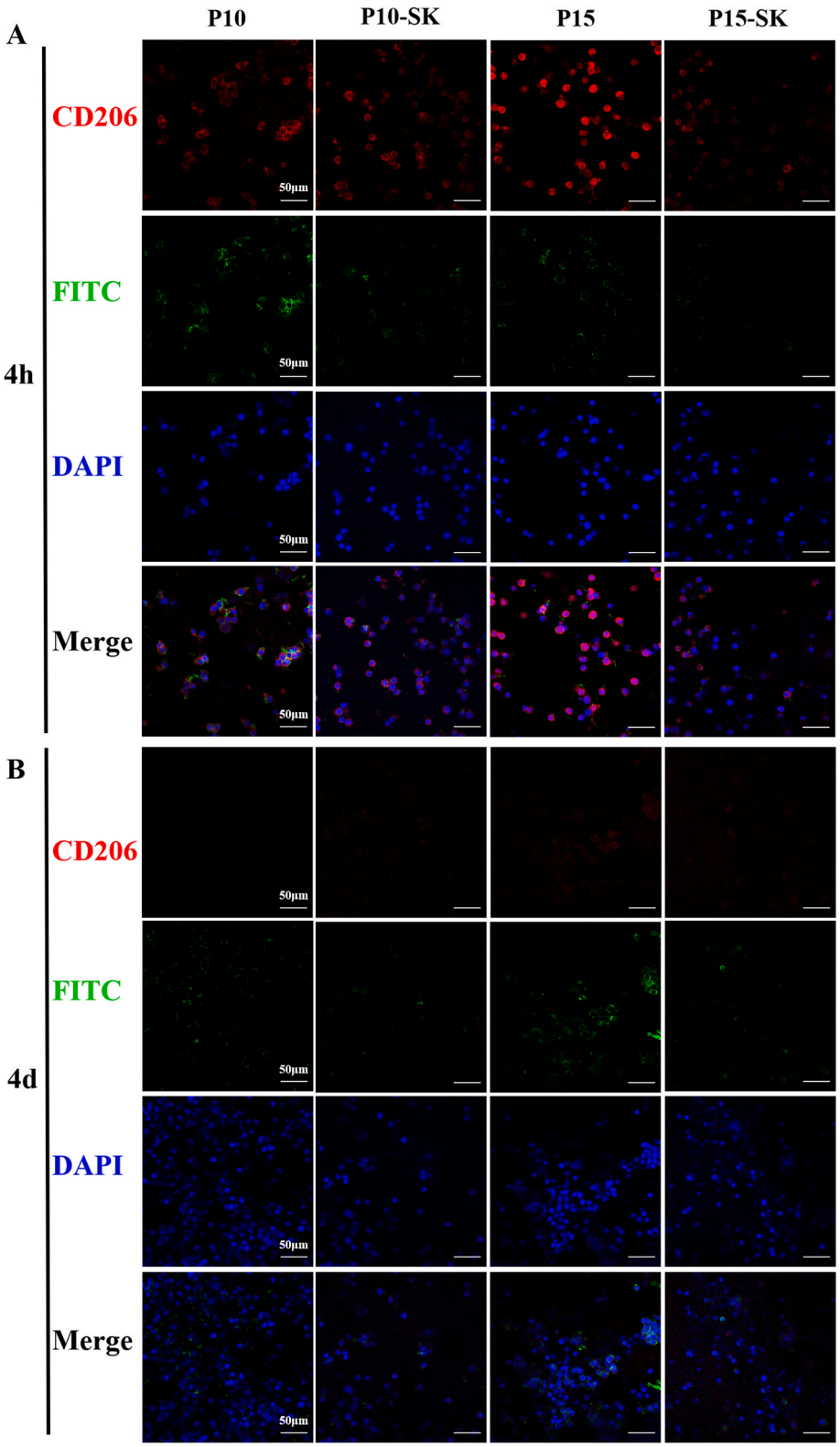

Fig. 4. Macrophage polarization on PCL fiber scaffolds of diverse structures. (A–B) Fluorescence staining of macrophage M2 polarization on fiber scaffolds with 4 h (A), 4 days (B). Red fluorescence intensity indicates the expression of M2 phenotype macrophage marker CD206, FITC-labeled ghost pen cyclic peptide-stained cytoskeleton (green), and DAPI-stained nuclei (blue). Scale bar: 50 μm.

around the fiber scaffolds (21 days). Tissue sections were stained for implanted fiber scaffolds at diverse time points. As demonstrated by H&E (Fig. 6A) and MT staining (Fig. 6B), there was dense infiltration of inflammatory cells in the tissue around the fiber scaffolds and myofibrillar tissue formation inside the fiber scaffolds. The collagen tissue around the P15 group was in the form of a scattered network, which ensured the possibility of material exchange between the fiber scaffolds and surrounding tissue. For the quantitative analysis of

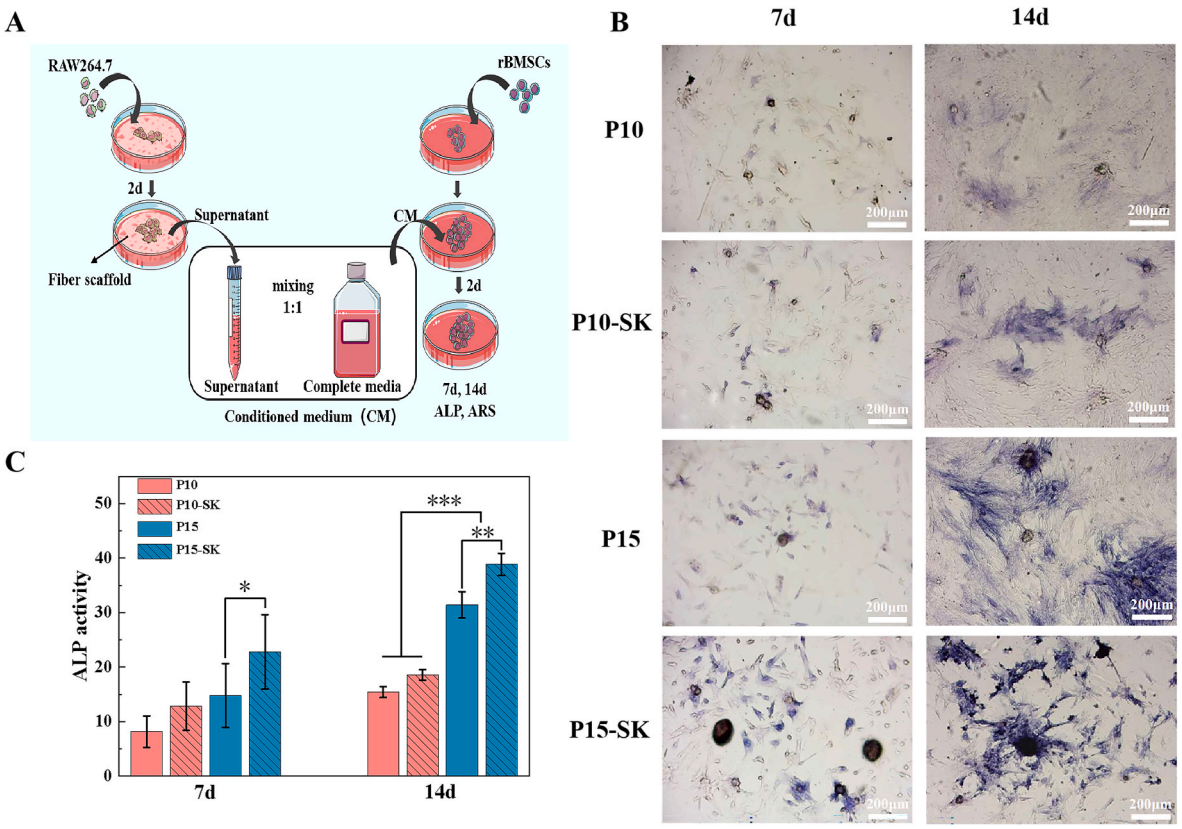

Fig. 5. Effect of macrophages on diverse structured PCL fiber scaffolds on osteogenic differentiation of rBMSCs. (A) Schematic diagram of the manipulation steps of the co-culture system (macrophages and stem cells), (B) ALP staining plot of CM on rBMSCs osteogenic differentiation by fiber scaffolds cultured macrophages, and (C) quantitative activity assay results. Scale bar: 200 μm *p < 0.05, **p < 0.01, ***p < 0.001.

collagen deposition (Fig. S8), less collagen was deposited on the large pore size and low-stiffness fiber scaffold P15-SK (16.51 %) compared to the smaller pore size and large-stiffness fiber scaffold P10, which had a mesh-like distribution of collagen structures with low density and good tissue regeneration.

To further evaluate the efficacy of the scaffolds in reducing the inflammatory response, we evaluated tissue sections of the fiber scaffolds by immunostaining with CD68 and CD206 antibodies to mark the infiltrative phenotype of macrophages around the fiber scaffolds and compute the number of infiltrated cells. Immunostaining of tissue sections of the implanted fiber scaffolds (Fig. 6C) and CD68-positive cells indicated a large infiltration and aggregation of macrophages around the fiber scaffolds in the P10 group. CD206-positive cells demonstrated the least infiltrated M2 phenotype macrophages in the P10 group and a significant increase in infiltrated M2 phenotype macrophages in the P15 group, with P15-SK reaching its maximum (1540 cells/mm^2) (Fig. 6D).

To verify the immunofluorescence and tissue staining results, qPCR was used to detect the expression levels of immune-related genes in macrophages in tissues 4 days after the *in vivo* implantation of PCL fiber scaffolds (Fig. 6E and F). The results demonstrated that the expression of IL-6 and IL-10 genes was higher and tended to be equal in P10, demonstrating anti-inflammatory and pro-inflammatory effects. The combination of immunofluorescence and tissue staining demonstrated that the fiber scaffold could regulate macrophage polarization, predominantly toward M1; P10-SK had neither pro-inflammatory nor anti-inflammatory effects, while both M1 and M2b macrophages secreted both genes (Table S3), and combined with immunofluorescence and it is reasonable to speculate that this type of fiber scaffold facilitates macrophage differentiation toward the M1 and M2b phenotypes. However, macrophages aggregated less on the large-pore-size and low-stiffness fiber scaffolds (P15 and P15-SK) and formed fewer FBGCs. The large pore size and low stiffness fiber scaffolds can create an anti-inflammatory microenvironment around the tissue; the presence of SK structures leads to increased roughness of the fiber scaffolds with superior immune properties and less macrophage aggregation and easier polarization toward the M2 phenotype, which has a positive impact on reducing inflammation.

3.6. The SK structured fiber scaffold mediated macrophage polarization

We prepared PCL fiber scaffolds with diverse diameters (0.10–5.00 μm) and pore sizes (1.78–12.50 μm) by electrospinning technique and formed SK nanostructures on the fiber surface by solution-induced crystallization method. It was demonstrated by *in vitro* macrophage co-culture that SK fiber scaffolds induced adhesion protein unfolding, cell adhesion, and cytokine expression, and macrophages demonstrated optimal M2 polarization on large pore size (12.50 μm) and low stiffness (5.62 MPa) P15 fiber scaffolds. A macrophage and stem cell co-culture system was constructed to mimic the *in vivo* tissue reconstruction microenvironment and the CM was able to continuously stimulate M2 macrophages and promote BMSCs differentiation into osteoblasts through paracrine effects. Subcutaneous transplantation trials in rats were conducted to validate the congruity between the inflammatory response and tissue regeneration of PCL fiber scaffolds with varying structures *in vitro* and *in vivo*. By utilizing HE and MT staining, along with CD68/CD206 positive cell profiles and qPCR analysis, it was verified that fiber scaffolds characterized by larger pore size and lower stiffness exhibited the capacity to induce an inflammatory microenvironment in the surrounding tissues. Additionally, the inclusion of SK structures led to heightened surface irregularities within the fiber scaffolds, thereby enhancing their immune performance. This structural modification also resulted in diminished macrophage aggregation and

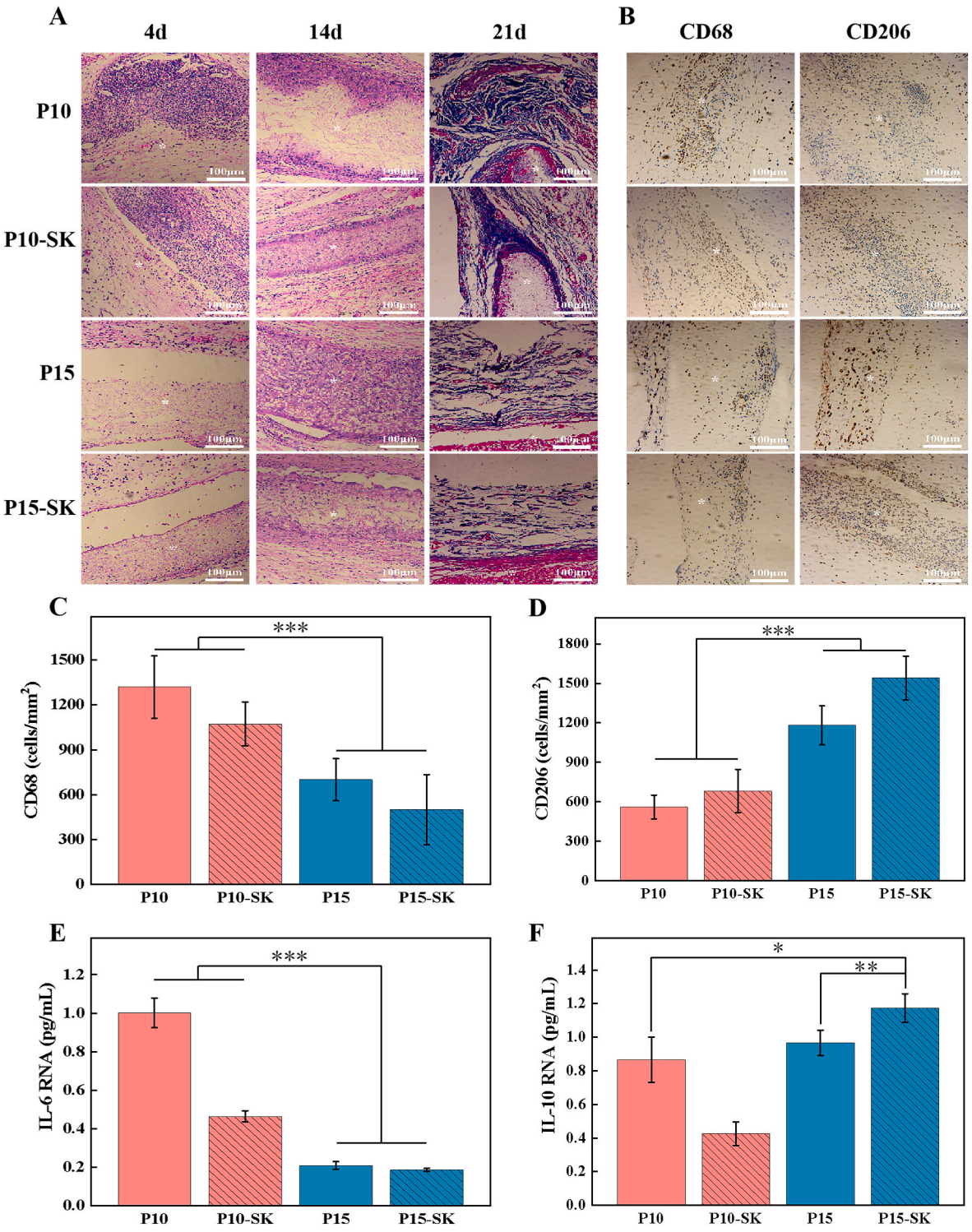

Fig. 6. Anti-inflammatory effect of diverse structured PCL fiber scaffolds *in vivo*. (A–B) H&E(A) and MT(B) staining of tissue sections of implanted fiber scaffolds, * represents fiber scaffolds cross-section. Scale bar: 100 μm. (C–D) Quantitative analysis of macrophages and M2 phenotype macrophages at 4 days, stained tissue sections of implanted fiber scaffolds with CD68(C) and CD206(D) antibodies. (E–F) Detection of immune-related gene IL-6(E) and IL-10(F) expression levels of macrophages in tissues 4 days post fiber scaffold implantation using qPCR. *$p < 0.05$, **$p < 0.01$, ***$p < 0.001$.

facilitated a more facile shift toward the M2 phenotype. This, in turn, results in favorable outcomes in terms of inflammation mitigation.

In this experiment, a few studies were conducted on the mechanism of macrophage adhesion and polarization induced by fiber scaffolds, and the electrospun fiber system was too complex for a single study on the effect of mechanical properties on the cell. Research indicates that integrins have the functionality of mechanical stress transduction, capable of activating appropriate mechanotransduction pathways in macrophages [53–55]. We hypothesize that the interaction between integrins on the surface of macrophages and the fiber scaffold transmits information from the morphological features of the material surface to the cells. The cells adapt their gene expression to achieve different function. It has been demonstrated that macrophages adjust their polarization state, cytokine secretion, and migration patterns according to

matrix material stiffness [56]. The mechanosensing steps, including periodic tests for changes in the substrate, substrate modification, and cellular protein content [57]. Initially, the cells sense the mechanical features of their environment and rapidly respond to motility and signals. While adapting to the environment, they also change it [58], altering the extracellular matrix and generating new signals, such as those from fibronectin unfolding, intracellular signals that change the cell expression pattern, and eventually the cell shape [59]. At any stage, extracellular signals, such as hormones or external mechanical stimuli [60], may cause drastic changes that trigger further cellular and matrix modifications.

Local responsiveness, geometry, and integration of all responses play imperative roles in gene expression regulation [61]. For synthetic surfaces, it is not only the geometry and rigidity but also the surface properties that ultimately control the composition and conformation of surface-adsorbed proteins [62]; therefore, this may be due to the synergistic effect of large pore size, low stiffness, and the SK structure inducing integrin-mediated cell signaling pathways. We also plan to further investigate the relevant molecular mechanisms in future work, conducting a more in-depth analysis of macrophage adhesion on the fiber scaffold and the expression of associated integrin genes. This will allow us to explore the mechanisms from the perspectives of mechanotransduction and signaling pathways.

4. Conclusion

In summary, we have successfully created electrospun fibers with varying diameters and introduced SK structures to the material surface using solution-induced crystallization. This process gave rise to SK-structured PCL fiber scaffolds with different pore sizes and surface roughness, enabling precise regulation of macrophage polarization. In vitro co-cultivation with macrophages demonstrated that SK-structured fibers enhance cell adhesion and effectively steer macrophage differentiation towards the M2 phenotype. Additionally, results from *in vitro* microenvironment simulations, mimicking *in vivo* tissue reconstruction, revealed that M2 macrophages promote the differentiation of bone marrow mesenchymal stem cells (BMSCs) into osteoblasts through paracrine effects. In rats implanted with a subcutaneous SK fiber scaffold, the large-pore-size and low-stiffness SK structured fiber scaffolds exhibited superior immune performance, with less macrophage aggregation and more polarization toward the anti-inflammatory M2 phenotype. Therefore, large pore sizes and low-stiffness SK fiber scaffolds guide the morphological design of in vivo-implanted biological scaffolds and are expected to be an effective strategy for the clinical application of graft materials to reduce inflammation.

CRediT authorship contribution statement

Gaowei Zhu: conceived and designed the experiments, performed the experiments, analyzed the data, prepared figures and/or tables. **Rongyan Zhang:** conceived and designed the experiments, performed the experiments, analyzed the data, prepared figures and/or tables. **Qianyang Xie:** performed the animal experiments and helped to prepare corresponding figures and/or tables., reviewed drafts of the paper, provided financial support, approved the final draft. **Peilun Li:** performed the animal experiments and helped to prepare corresponding figures and/or tables.. **Fujun Wang:** reviewed drafts of the paper, provided financial support, approved the final draft. **Lu Wang:** reviewed drafts of the paper, provided financial support, approved the final draft. **Chaojing Li:** conceived and designed the experiments, reviewed drafts of the paper, provided financial support, approved the final draft.

Declaration of competing interest

The authors declare that they have no known competing financial interests or personal relationships that could have appeared to influence the work reported in this paper.

Data availability

Data will be made available on request.

Acknowledgement

This work was supported by the National Natural Science Foundation of China (NSFC) (32201080), Shanghai Science and Technology Development Fund (21S31900700), 111 Project 2.0 (Grant No. BP0719035), the Special project for clinical research of Shanghai municipal Health Commission (Grant No. 20204Y0459).

Appendix A. Supplementary data

Supplementary data to this article can be found online at https://doi.org/10.1016/j.mtbio.2023.100880.

References

[1] R.V. Gayet, H. de Puig, M.A. English, L.R. Soenksen, P.Q. Nguyen, A.S. Mao, N. M. Angenent-Mari, J.J. Collins, Creating CRISPR-responsive smart materials for diagnostics and programmable cargo release, Nat. Protoc. 15 (9) (2020) 3030–3063, https://doi.org/10.1038/s41596-020-0367-8.

[2] W. Ling, G. Liew, Y. Li, Y. Hao, H. Pan, H. Wang, B. Ning, H. Xu, X. Huang, Materials and techniques for implantable nutrient sensing using flexible sensors integrated with metal–organic frameworks, Adv. Mater. 30 (23) (2018), 1800917, https://doi.org/10.1002/adma.201800917.

[3] S. Borandeh, B. van Bochove, A. Teotia, J. Seppälä, Polymeric drug delivery systems by additive manufacturing, Adv. Drug Deliv. Rev. 173 (2021) 349–373, https://doi.org/10.1016/j.addr.2021.03.022.

[4] D. Zhi, Q. Cheng, A.C. Midgley, Q. Zhang, T. Wei, Y. Li, T. Wang, T. Ma, M. Rafique, S. Xia, Y. Cao, Y. Li, J. Li, Y. Che, M. Zhu, K. Wang, D. Kong, Mechanically reinforced biotubes for arterial replacement and arteriovenous grafting inspired by architectural engineering, Sci. Adv. 8 (11) (2022), eabl3888, https://doi.org/10.1126/sciadv.abl3888.

[5] H.S. Kim, S.G. Kumbar, S.P. Nukavarapu, Amorphous silica fiber matrix biomaterials: an analysis of material synthesis and characterization for tissue engineering, Bioact. Mater. 19 (2023) 155–166, https://doi.org/10.1016/j.bioactmat.2022.04.002.

[6] J.M. Belloń, L.A. Contreras, G. Pascual, J. Bujań, Evaluation of the acute scarring response to the implant of different types of biomaterial in the abdominal wall, J. Mater. Sci. Mater. Med. 11 (1) (2000) 25–29, https://doi.org/10.1023/A:1008981517743.

[7] J. Han, Y.S. Kim, M.-Y. Lim, H.Y. Kim, S. Kong, M. Kang, Y.W. Choo, J.H. Jun, S. Ryu, H.-y. Jeong, J. Park, G.-J. Jeong, J.-C. Lee, G.H. Eom, Y. Ahn, B.-S. Kim, Dual roles of graphene oxide to attenuate inflammation and elicit timely polarization of macrophage phenotypes for cardiac repair, ACS Nano 12 (2) (2018) 1959–1977, https://doi.org/10.1021/acsnano.7b09107.

[8] R. Klopfleisch, Macrophage reaction against biomaterials in the mouse model – phenotypes, functions and markers, Acta Biomater. 43 (2016) 3–13, https://doi.org/10.1016/j.actbio.2016.07.003.

[9] J.J. O'Shea, P.J. Murray, Cytokine signaling modules in inflammatory responses, Immunity 28 (4) (2008) 477–487, https://doi.org/10.1016/j.immuni.2008.03.002.

[10] I. Amit, D.R. Winter, S. Jung, Correction: corrigendum: the role of the local environment and epigenetics in shaping macrophage identity and their effect on tissue homeostasis, Nat. Immunol. 18 (2) (2017), https://doi.org/10.1038/ni0217-246b, 246-246.

[11] L. Ma, W. Li, Y. Zhang, L. Qi, Q. Zhao, N. Li, Y. Lu, L. Zhang, F. Zhou, Y. Wu, Y. He, H. Yu, Y. He, B. Wei, H. Wang, FLT4/VEGFR3 activates AMPK to coordinate glycometabolic reprogramming with autophagy and inflammasome activation for bacterial elimination, Autophagy 18 (6) (2022) 1385–1400, https://doi.org/10.1080/15548627.2021.1985338.

[12] S. Liu, H. Chen, T. Wu, G. Pan, C. Fan, Y. Xu, W. Cui, Macrophage infiltration of electrospun polyester fibers, Biomater. Sci. 5 (8) (2017) 1579–1587, https://doi.org/10.1039/C6BM00958A.

[13] I. Cockerill, Y. Su, J.H. Lee, D. Berman, M.L. Young, Y. Zheng, D. Zhu, Micro-/nanotopography on bioresorbable zinc dictates cytocompatibility, bone cell differentiation, and macrophage polarization, Nano Lett. 20 (6) (2020) 4594–4602, https://doi.org/10.1021/acs.nanolett.0c01448.

[14] T. Maehara, K. Fujimori, Contribution of FP receptors in M1 macrophage polarization via IL-10-regulated nuclear translocation of NF-κB p65, Biochim. Biophys. Acta Mol. Cell Biol. Lipids 1865 (5) (2020), 158654, https://doi.org/10.1016/j.bbalip.2020.158654.

[15] S. Gao, J. Zhou, N. Liu, L. Wang, Q. Gao, Y. Wu, Q. Zhao, P. Liu, S. Wang, Y. Liu, Curcumin induces M2 macrophage polarization by secretion IL-4 and/or IL-13, J. Mol. Cell. Cardiol. 85 (2015) 131–139, https://doi.org/10.1016/j.yjmcc.2015.04.025.

[16] H. Xu, Y. Zhu, A.W.-T. Hsiao, J. Xu, W. Tong, L. Chang, X. Zhang, Y.-F. Chen, J. Li, W. Chen, Bioactive glass-elicited stem cell-derived extracellular vesicles regulate M2 macrophage polarization and angiogenesis to improve tendon regeneration and functional recovery, Biomaterials 294 (2023), 121998, https://doi.org/10.1016/j.biomaterials.2023.121998.
[17] Y. Zhu, H. Liang, X. Liu, J. Wu, C. Yang, T.M. Wong, K.Y. Kwan, K.M. Cheung, S. Wu, K.W. Yeung, Regulation of macrophage polarization through surface topography design to facilitate implant-to-bone osteointegration, Sci. Adv. 7 (14) (2021), eabf6654, https://doi.org/10.1126/sciadv.abf6654.
[18] J. Xie, X. Wu, S. Zheng, K. Lin, J. Su, Aligned electrospun poly (L-lactide) nanofibers facilitate wound healing by inhibiting macrophage M1 polarization via the JAK-STAT and NF-κB pathways, J. Nanobiotechnol. 20 (1) (2022) 342, https://doi.org/10.1186/s12951-022-01549-9.
[19] S. Wu, T. Dong, Y. Li, M. Sun, Y. Qi, J. Liu, M.A. Kuss, S. Chen, B. Duan, State-of-the-art review of advanced electrospun nanofiber yarn-based textiles for biomedical applications, Appl. Mater. Today 27 (2022), 101473, https://doi.org/10.1016/j.apmt.2022.101473.
[20] J. Voorneveld, A. Oosthuysen, T. Franz, P. Zilla, D. Bezuidenhout, Dual electrospinning with sacrificial fibers for engineered porosity and enhancement of tissue ingrowth, J. Biomed. Mater. Res. B Appl. Biomater. 105 (6) (2017) 1559–1572, https://doi.org/10.1002/jbm.b.33695.
[21] R. Scaffaro, E.F. Gulino, M.C. Citarrella, Biodegradable membrane with high porosity and hollow structure obtained via electrospinning for oil spill clean-up application, J. Polym. Environ. 31 (9) (2023) 3965–3981, https://doi.org/10.1007/s10924-023-02876-0.
[22] Z. Huang, Y. Zhang, R. Liu, Y. Li, M. Rafique, A.C. Midgley, Y. Wan, H. Yan, J. Si, T. Wang, C. Chen, P. Wang, M. Shafiq, J. Li, L. Zhao, D. Kong, K. Wang, Cobalt loaded electrospun poly(ε-caprolactone) grafts promote antibacterial activity and vascular regeneration in a diabetic rat model, Biomaterials 291 (2022), 121901, https://doi.org/10.1016/j.biomaterials.2022.121901.
[23] Y. Zhang, K. Xu, D. Zhi, M. Qian, K. Liu, Q. Shuai, Z. Qin, J. Xie, K. Wang, J. Yang, Improving vascular regeneration performance of electrospun poly(ε-caprolactone) vascular grafts via synergistic functionalization with VE-cadherin/VEGF, Advanced Fiber Materials 4 (6) (2022) 1685–1702, https://doi.org/10.1007/s42765-022-00213-z.
[24] Y. Li, J. Wang, D. Qian, L. Chen, X. Mo, L. Wang, Y. Wang, W. Cui, Electrospun fibrous sponge via short fiber for mimicking 3D ECM, J. Nanobiotechnol. 19 (1) (2021) 131, https://doi.org/10.1186/s12951-021-00878-5.
[25] X. Xie, Y. Chen, X. Wang, X. Xu, Y. Shen, A.u.R. Khan, A. Aldalbahi, A.E. Fetz, G. L. Bowlin, M. El-Newehy, X. Mo, Electrospinning nanofiber scaffolds for soft and hard tissue regeneration, J. Mater. Sci. Technol. 59 (2020) 243–261, https://doi.org/10.1016/j.jmst.2020.04.037.
[26] G. Sahin, E. Vrij, R. Grant, S. Giselbrecht, The Synergy of Electrospinning and Imprinting for Faithful Replication of Fiber Structures, Advanced Materials Technologies n/a(n/a) (2020), https://doi.org/10.1002/admt.202300344, 2300344.
[27] M. Bartneck, K.-H. Heffels, Y. Pan, M. Bovi, G. Zwadlo-Klarwasser, J. Groll, Inducing healing-like human primary macrophage phenotypes by 3D hydrogel coated nanofibres, Biomaterials 33 (16) (2012) 4136–4146, https://doi.org/10.1016/j.biomaterials.2012.02.050.
[28] T. Tylek, C. Blum, A. Hrynevich, K. Schlegelmilch, T. Schilling, P.D. Dalton, J. Groll, Precisely defined fiber scaffolds with 40 μm porosity induce elongation driven M2-like polarization of human macrophages, Biofabrication 12 (2) (2020), 025007, https://doi.org/10.1088/1758-5090/ab5f4e.
[29] M.J. Vassey, G.P. Figueredo, D.J. Scurr, A.S. Vasilevich, S. Vermeulen, A. Carlier, J. Luckett, N.R.M. Beijer, P. Williams, D.A. Winkler, J. de Boer, A. M. Ghaemmaghami, M.R. Alexander, Immune modulation by design: using topography to control human monocyte attachment and macrophage differentiation, Adv. Sci. 7 (11) (2020), 1903392, https://doi.org/10.1002/advs.201903392.
[30] Q. Zhang, J.W. Hwang, J.-H. Oh, C.H. Park, S.H. Chung, Y.-S. Lee, J.-H. Baek, H.-M. Ryoo, K.M. Woo, Effects of the fibrous topography-mediated macrophage phenotype transition on the recruitment of mesenchymal stem cells: an in vivo study, Biomaterials 149 (2017) 77–87, https://doi.org/10.1016/j.biomaterials.2017.10.007.
[31] C. Chen, Y. Chen, Y.-j. Lan, M.-n. Tian, Y.-m. Zhang, Z.-y. Lei, D.-l. Fan, Effects of substrate topography on the regulation of human fibroblasts and capsule formation via modulating macrophage polarization, Colloids Surf. B Biointerfaces 222 (2023), 113086, https://doi.org/10.1016/j.colsurfb.2022.113086.
[32] N.J. Schaub, A.R. D'Amato, A. Mason, D.T. Corr, E.Y. Harmon, M.R. Lennartz, R. J. Gilbert, The effect of engineered nanotopography of electrospun microfibers on fiber rigidity and macrophage cytokine production, J. Biomater. Sci. Polym. Ed. 28 (13) (2017) 1303–1323, https://doi.org/10.1080/09205063.2017.1321345.
[33] M. Douglass, M. Garren, R. Devine, A. Mondal, H. Handa, Bio-inspired hemocompatible surface modifications for biomedical applications, Prog. Mater. Sci. 130 (2022), 100997, https://doi.org/10.1016/j.pmatsci.2022.100997.
[34] A. Venugopal, L.H.T. Egberts, J. Meeprasert, E.A. Pidko, B. Dam, T. Burdyny, V. Sinha, W.A. Smith, Polymer modification of surface electronic properties of electrocatalysts, ACS Energy Lett. 7 (5) (2022) 1586–1593, https://doi.org/10.1021/acsenergylett.2c00199.
[35] S.M. Pasini, A. Valério, S.M.A. Guelli Ulson de Souza, D. Hotza, G. Yin, J. Wang, A. A. Ulson de Souza, Plasma-modified TiO2/polyetherimide nanocomposite fibers for photocatalytic degradation of organic compounds, J. Environ. Chem. Eng. 7 (4) (2019), 103213, https://doi.org/10.1016/j.jece.2019.103213.
[36] X. Chen, B. Dong, B. Wang, R. Shah, C.Y. Li, Crystalline block copolymer decorated, hierarchically ordered polymer nanofibers, Macromolecules 43 (23) (2010) 9918–9927, https://doi.org/10.1021/ma101900n.
[37] W. Han, G. Zheng, Y. Liang, K. Dai, C. Liu, J. Chen, C. Shen, X. Peng, P. Fu, W. Cao, Q. Li, HDPE solution crystallization induced by electrospun PA66 nanofiber, Colloid Polym. Sci. 289 (7) (2011) 843–848, https://doi.org/10.1007/s00396-011-2389-9.
[38] X. Jing, H.-Y. Mi, X.-C. Wang, X.-F. Peng, L.-S. Turng, Shish-kebab-structured poly (ε-caprolactone) nanofibers hierarchically decorated with chitosan–poly (ε-caprolactone) copolymers for bone tissue engineering, ACS Appl. Mater. Interfaces 7 (12) (2015) 6955–6965, https://doi.org/10.1021/acsami.5b00900.
[39] B. Dong, Y. Guo, S. Sun, H.-Y. Mi, P. He, M.F. Antwi-Afari, C. Liu, C. Shen, Shish–kebab-structured UHMWPE coating for efficient and cost-effective oil–water separation, ACS Appl. Mater. Interfaces 12 (52) (2020) 58252–58262, https://doi.org/10.1021/acsami.0c17900.
[40] M. Bartnikowski, T.R. Dargaville, S. Ivanovski, D.W. Hutmacher, Degradation mechanisms of polycaprolactone in the context of chemistry, geometry and environment, Prog. Polym. Sci. 96 (2019) 1–20, https://doi.org/10.1016/j.progpolymsci.2019.05.004.
[41] E. Altrock, C.A. Muth, G. Klein, J.P. Spatz, C. Lee-Thedieck, The significance of integrin ligand nanopatterning on lipid raft clustering in hematopoietic stem cells, Biomaterials 33 (11) (2012) 3107–3118, https://doi.org/10.1016/j.biomaterials.2012.01.002.
[42] C. Drosou, M. Krokida, C.G. Biliaderis, Composite pullulan-whey protein nanofibers made by electrospinning: impact of process parameters on fiber morphology and physical properties, Food Hydrocolloids 77 (2018) 726–735, https://doi.org/10.1016/j.foodhyd.2017.11.014.
[43] A. Padhi, A.S. Nain, ECM in differentiation: a review of matrix structure, composition and mechanical properties, Ann. Biomed. Eng. 48 (3) (2020) 1071–1089, https://doi.org/10.1007/s10439-019-02337-7.
[44] C. Zhang, L. Qian, H. Zhao, Elucidation of regional mechanical properties of brain tissues based on cell density, JBE 18 (3) (2021) 611–622, https://doi.org/10.1007/s42235-021-0047-6.
[45] W. Chen, D.-H. Kim, C.T. Lim, Special issue: biomaterials for cell mechanobiology, ACS Biomater. Sci. Eng. 5 (8) (2019) 3685–3687, https://doi.org/10.1021/acsbiomaterials.9b01123.
[46] R. Sridharan, A.R. Cameron, D.J. Kelly, C.J. Kearney, F.J. O'Brien, Biomaterial based modulation of macrophage polarization: a review and suggested design principles, Mater. Today 18 (6) (2015) 313–325, https://doi.org/10.1016/j.mattod.2015.01.019.
[47] I. Lynch, A. Salvati, K.A. Dawson, What does the cell see? Nat. Nanotechnol. 4 (9) (2009) 546–547, https://doi.org/10.1038/nnano.2009.248.
[48] Y. Pan, Y. Qi, N. Shao, A.C. Tadle, Y. Huang, Amino-modified polymer nanoparticles as adjuvants to activate the complement system and to improve vaccine efficacy in vivo, Biomacromolecules 20 (9) (2019) 3575–3583, https://doi.org/10.1021/acs.biomac.9b00887.
[49] Y. Liu, X. Wan, Y. Yuan, J. Huang, Y. Jiang, K. Zhao, Y. Wang, Y. Liu, Q. Wang, H. Jin, Opposite effects of miR-155 in the initial and later stages of lipopolysaccharide (LPS)-induced inflammatory response, J. Zhejiang Univ. - Sci. B 22 (7) (2021) 590–598, https://doi.org/10.1631/jzus.B2000826.
[50] D. Kyurkchiev, I. Bochev, E. Ivanova-Todorova, M. Mourdjeva, T. Oreshkova, K. Belemezova, S. Kyurkchiev, Secretion of immunoregulatory cytokines by mesenchymal stem cells, World J. Stem Cell. 6 (5) (2014) 552, https://doi.org/10.4252/wjsc.v6.i5.552.
[51] J. Pajarinen, T. Lin, E. Gibon, Y. Kohno, M. Maruyama, K. Nathan, L. Lu, Z. Yao, S. B. Goodman, Mesenchymal stem cell-macrophage crosstalk and bone healing, Biomaterials 196 (2019) 80–89, https://doi.org/10.1016/j.biomaterials.2017.12.025.
[52] C.M. Madl, S.C. Heilshorn, H.M. Blau, Bioengineering strategies to accelerate stem cell therapeutics, Nature 557 (7705) (2018) 335–342, https://doi.org/10.1038/s41586-018-0089-z.
[53] S. Seetharaman, B. Vianay, V. Roca, A.J. Farrugia, C. De Pascalis, B. Boëda, F. Dingli, D. Loew, S. Vassilopoulos, A. Bershadsky, M. Théry, S. Etienne-Manneville, Microtubules tune mechanosensitive cell responses, Nat. Mater. 21 (3) (2022) 366–377, https://doi.org/10.1038/s41563-021-01108-x.
[54] T.D. Zaveri, J.S. Lewis, N.V. Dolgova, M.J. Clare-Salzler, B.G. Keselowsky, Integrin-directed modulation of macrophage responses to biomaterials, Biomaterials 35 (11) (2014) 3504–3515, https://doi.org/10.1016/j.biomaterials.2014.01.007.
[55] L. Lv, Y. Xie, K. Li, T. Hu, X. Lu, Y. Cao, X. Zheng, Unveiling the mechanism of surface hydrophilicity-modulated macrophage polarization, Adv. Healthcare Mater. 7 (19) (2018), 1800675, https://doi.org/10.1002/adhm.201800675.
[56] M. Chen, Y. Zhang, P. Zhou, X. Liu, H. Zhao, X. Zhou, Q. Gu, B. Li, X. Zhu, Q. Shi, Substrate stiffness modulates bone marrow-derived macrophage polarization through NF-κB signaling pathway, Bioact. Mater. 5 (4) (2020) 880–890, https://doi.org/10.1016/j.bioactmat.2020.05.004.
[57] V. Vogel, M. Sheetz, Local force and geometry sensing regulate cell functions, Nat. Rev. Mol. Cell Biol. 7 (4) (2006) 265–275, https://doi.org/10.1038/nrm1890.
[58] Y. Liu, T. Segura, Biomaterials-mediated regulation of macrophage cell fate, Front. Bioeng. Biotechnol. 8 (2020), https://doi.org/10.3389/fbioe.2020.609297.
[59] V. Nascimento Da Conceicao, Y. Sun, K. Ramachandran, A. Chauhan, A. Raveendran, M. Venkatesan, B. DeKumar, S. Maity, N. Vishnu, G.A. Kotsakis, P. F. Worley, D.L. Gill, B.B. Mishra, M. Madesh, B.B. Singh, Resolving macrophage polarization through distinct Ca2+ entry channel that maintains intracellular signaling and mitochondrial bioenergetics, iScience 24 (11) (2021), 103339, https://doi.org/10.1016/j.isci.2021.103339.

[60] Y. Xia, S. Chen, S. Zeng, Y. Zhao, C. Zhu, B. Deng, G. Zhu, Y. Yin, W. Wang, R. Hardeland, W. Ren, Melatonin in macrophage biology: current understanding and future perspectives, J. Pineal Res. 66 (2) (2019), e12547, https://doi.org/10.1111/jpi.12547.

[61] R. Sridharan, B. Cavanagh, A.R. Cameron, D.J. Kelly, F.J. O'Brien, Material stiffness influences the polarization state, function and migration mode of macrophages, Acta Biomater. 89 (2019) 47–59, https://doi.org/10.1016/j.actbio.2019.02.048.

[62] D. Faulón Marruecos, D.K. Schwartz, J.L. Kaar, Impact of surface interactions on protein conformation, Curr. Opin. Colloid Interface Sci. 38 (2018) 45–55, https://doi.org/10.1016/j.cocis.2018.08.002.